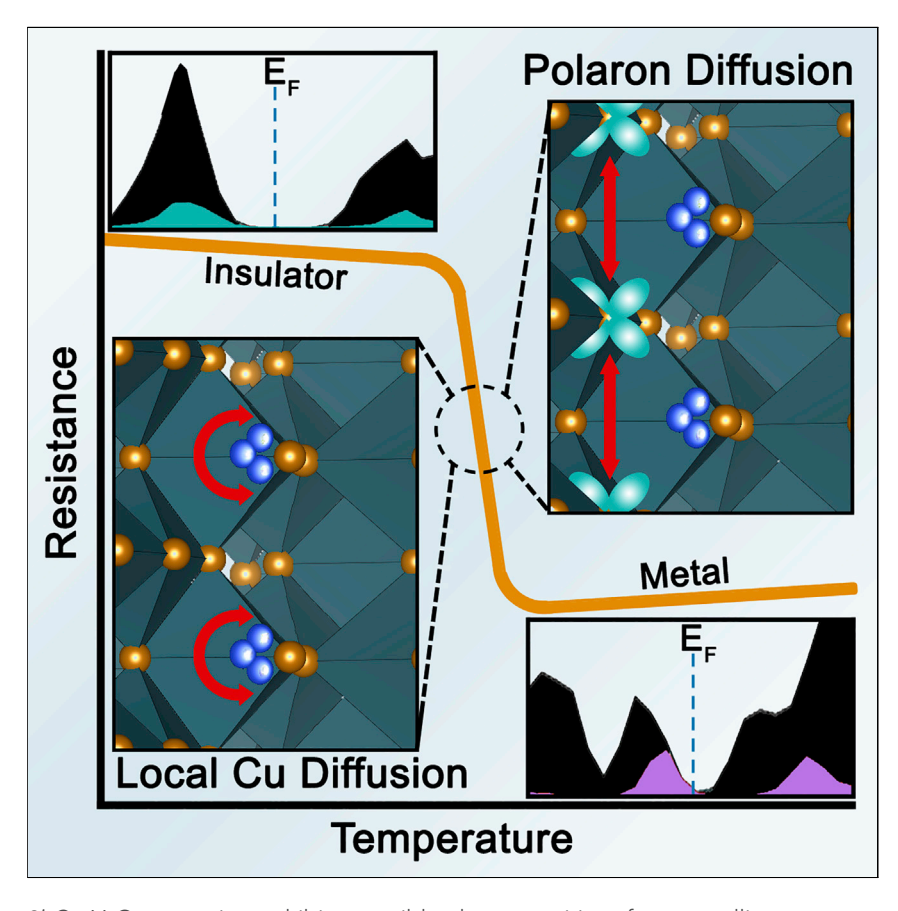
Matter Cell Press

Article

Metal-Insulator Transitions in β' -Cu_xV₂O₅ Mediated by Polaron Oscillation and Cation Shuttling



 $\beta'\text{-}Cu_xV_2O_5$ nanowires exhibit reversible phase transitions from metallic to insulating states (i.e., a metal-insulator transition, MIT). Unlike in VO_2 where the MIT derives in part from a structural transition, the MIT in $\beta'\text{-}Cu_xV_2O_5$ is primarily an electronic phase transition. Here we show that the transition is underpinned by the diffusion of copper between two closely related sites, which drives polaron oscillation on the V_2O_5 sublattice. This distinctive mechanism represents an intriguing approach to engineering energy-efficient MITs for neuromorphic computing applications.

Abhishek Parija, Joseph V. Handy, Justin L. Andrews, ..., R. Stanley Williams, David Prendergast, Sarbajit Banerjee

rstanleywilliams@tamu.edu (R.S.W.) dgprendergast@lbl.gov (D.P.) banerjee@chem.tamu.edu (S.B.)

HIGHLIGHTS

 β' -Cu_xV₂O₅ exhibits temperature-, voltage-, and field-driven metalinsulator transitions

Diffusion of Cu facilitates the oscillation of polarons between adjacent vanadium sites

Polaron oscillation and delocalization leads to metallization, triggering an MIT

Close coupling of ionic and polaronic diffusion can be used for neuromorphic computing



Parija et al., Matter *2*, 1–21 April 1, 2020 © 2020 Elsevier Inc. https://doi.org/10.1016/j.matt.2020.01.027

CellPress

Article

Metal-Insulator Transitions in β'-Cu_xV₂O₅ Mediated by Polaron Oscillation and Cation Shuttling

Abhishek Parija, ^{1,2,3,4,9} Joseph V. Handy, ^{1,2,9} Justin L. Andrews, ^{1,2,9} Jinpeng Wu, ⁴ Linda Wangoh, ⁵ Sujay Singh, ⁶ Chris Jozwiak, ⁴ Aaron Bostwick, ⁴ Eli Rotenberg, ⁴ Wanli Yang, ⁴ Sirine C. Fakra, ⁴ Mohammed Al-Hashimi, ⁷ G. Sambandamurthy, ⁶ Louis F.J. Piper, ⁵ R. Stanley Williams, ^{8,*} David Prendergast, ^{3,*} and Sarbajit Banerjee^{1,2,10,11,*}

SUMMARY

Silicon circuitry has dominated the semiconductor industry for decades but is constrained in its power efficiency by the Fermi-Dirac distribution of electron energies. Electron-correlated transition metal oxides exhibiting metal-to-insulator transitions (MITs) are excellent candidates for energy-efficient computation, which can further emulate the spiking behavior of biological neural circuitry. We demonstrate that $\beta'\text{-}Cu_xV_2O_5$ exhibits a pronounced nonlinear response to applied temperature, voltage, and current, and the response can be modulated as a function of Cu stoichiometry. We show that polaron oscillation, coupled to the real-space shuttling of Cu ions across two adjacent sites, underpins the MIT of this material. These results reveal the interplay between crystal structure distortions and electron correlation in underpinning the metal-insulator transition of a strongly correlated system. The utilization of coupled cation diffusion and polaron oscillation further demonstrates a means of using ionic vectors to obtain highly nonlinear conductance switching as required for neuromorphic computing.

INTRODUCTION

Complementary metal-oxide-semiconductor field-effect transistors constructed from silicon have long been the workhorse of computing architectures, and their scaling to ever smaller dimensions has underpinned a far-reaching revolution in computational power, capacity, and cost. 1-4 However, the performance of silicon circuitry is fundamentally constrained by the Fermi-Dirac electron distribution of electron energies, which establishes a 60-mV/decade limit to the steepness of switching characteristics upon application of a gate voltage at room temperature. 1 The shallow slopes of electrostatically modulated transistors lead to wasted power consumption and are the genesis of "dark silicon," the practice of leaving large swathes of logic circuitry on a chip inoperative at any given time in order to prevent the circuit overheating. To mitigate this challenge, which has upended Moore's scaling, the utilization of steep-slope switches has been proposed, 5-7 wherein a small change in voltage induces a large modulation of current.

Electron-correlated transition metal oxides exhibiting pronounced metal-insulator transitions (MITs) are excellent candidates for steep-slope transistors and further provide a means to emulate the spiking behavior of biological neural circuitry within

Progress and Potential

Since ca. 2006, silicon-based transistors have been operating at the thermodynamic limit of their power efficiency. For computing power to continue improving at a pace as required to underpin the development of advanced, energy-efficient technologies, a new computing paradigm is required. One approach, neuromorphic computing, aims to emulate the functionality of the human brain using solid-state materials, thereby imitating the efficiency and pattern-recognition capabilities exhibited by the synaptic architectures of the brain. Employing metal-insulator transitions (MITs), whereby a single material undergoes a reversible phase transition from an insulating to a conducting state, represents one possible means of achieving this goal. We show that local diffusion and closely coupled polaron oscillation are critical in driving the MIT in β' -Cu_xV₂O₅. Our research details a new mechanism and further elucidates materials design principles for neuromorphic computing applications.



neuromorphic architectures.⁸ Much attention has focused on the search for materials exhibiting large conductance switching but with relatively small lattice distortions and greater tunability of the transformation temperature.⁹ Here, we identify a coupled polaron oscillation and cation-shuttling mechanism as the origin of thermally triggered and voltage/current-driven metal-insulator transitions in a family of quasi-one-dimensional (1D) tunnel-structured materials, β' -Cu_xV₂O₅, where x represents the variable stoichiometry of Cu ions (0.27 < x < 0.67). Such a mechanism points to an entirely distinctive approach to the design of materials exhibiting programmable electronic instabilities as required for neuromorphic electronics.

Ternary vanadium oxides (M_xV₂O₅) represent a diverse palette of compounds spanning many low-dimensional structural motifs that are capable of accommodating cations (M) drawn from across the s- and p-blocks as well as transition metals at widely ranging stoichiometries (x). 10-14 Upon insertion of cations, electrons are donated from the intercalated ion, M, to the formally $d^0 V_2 O_5$ framework. Consequently, electron correlation along such frameworks can be sensitively tuned as a function of structure and composition, and has further been shown to underpin the manifestation of phenomena such as memristive switching, ¹⁵ low-temperature spin gaps, 16 pressure-induced superconductivity, 17 and MITs. $^{10,18-23}$ β' -Cu_xV₂O₅ is characterized by a pronounced MIT, the critical transition temperature (T_c) and magnitude of which have been found to depend sensitively on the Cu stoichiometry, $x.^{10,21-23}$ In contrast to the canonical MIT material, VO_2 , in which both Mott and Peierls mechanisms have been implicated as the underlying origin of the MIT (but considerable new insight has emerged from recent studies), 24-26 little is known about the precise mechanistic origins of the observed electronic instabilities in ternary vanadium oxides. 9,14 Cu concomitantly donates a valence electron to the V_2O_5 lattice upon insertion into the V_2O_5 framework. The localization of the electron on a specific vanadium site within the V_2O_5 framework induces a pronounced local structural distortion as extensively documented for Li-ion insertion in α -V₂O₅. ²⁷⁻²⁹ The coupling between the localized electron and the local structural distortion (which further tends to be approximately on the scale of a single unit cell) is termed a small polaron. Further coupling between the intercalated cationic species and the polaron has been observed in V₂O₅ systems, resulting in a polaron that is "self-trapped" in proximity to a positively charged ion, which has been documented extensively in $\text{Li}_x\text{V}_2\text{O}_5$ and $\text{Mg}_x\text{V}_2\text{O}_5$ cathode materials. ^{28–34} A similar scenario is envisioned upon monovalent Cu insertion with the cation trapped by interactions with the resulting small polaron derived from electron localization.

Herein, we show that polaron oscillation (i.e., the back-and-forth diffusion) between neighboring vanadium sites is strongly coupled to the real-space shuttling of Cu ions between two adjacent crystallographic sites. Notably, this mechanism is entirely distinct from Li_xV₂O₅ and Mg_xV₂O₅ self-trapped polaron systems wherein continuous polaron diffusion along the tunnels is observed. Such a coupled shuttling motion of the Cu ion and small polaron narrows the effective band gap of β' -Cu_xV₂O₅ and underpins metallization at high temperatures. Detailed analysis of high-resolution synchrotron powder diffraction, single-crystal diffraction, and extended X-ray absorption fine structure (EXAFS) reveals that with increasing temperature, Cu ions more readily shuttle between two crystallographically distinct sites. Spectroscopic studies of the electronic structure, probing both valence and conduction band states of β' -Cu_xV₂O₅ as a function of composition and temperature, provide clear evidence for polaronic states, which are stabilized on vanadium sites at low temperature but are delocalized at elevated temperatures coincident with the MIT observed in transport data. Molecular dynamics (MD) and nudged elastic band

¹Department of Chemistry, Texas A&M University, College Station, TX 77843, USA

²Department of Material Science and Engineering, Texas A&M University, College Station, TX 77843, USA

³The Molecular Foundry, Lawrence Berkeley National Laboratory, Berkeley, CA 94720, USA

⁴Advanced Light Source, Lawrence Berkeley National Laboratory, Berkeley, CA 94720, USA

⁵Department of Physics, Applied Physics and Astronomy, Binghamton University, Binghamton, NY 13902. USA

⁶Department of Physics, University at Buffalo, State University of New York, Buffalo, NY 14260, USA

⁷Department of Chemistry, Texas A&M University at Qatar, P.O. Box 23874, Doha, Qatar

⁸Department of Electrical and Computer Engineering, Texas A&M University, College Station, TX 77843, USA

⁹These authors contributed equally

¹⁰Twitter: @SarbajitBanerj1

rstanleywilliams@tamu.edu (R.S.W.), dgprendergast@lbl.gov (D.P.), banerjee@chem.tamu.edu (S.B.)

https://doi.org/10.1016/j.matt.2020.01.027

¹¹Lead Contact

^{*}Correspondence:

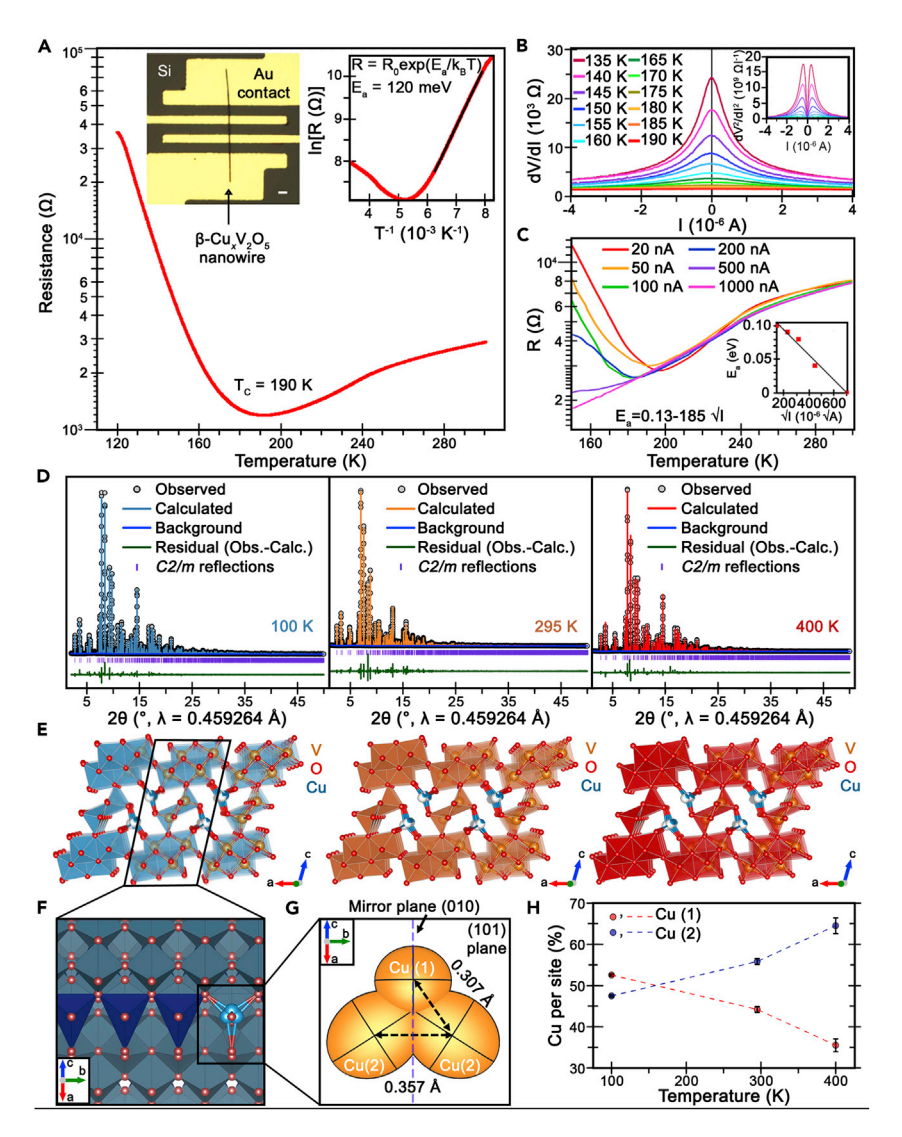


Figure 1. Electronic Phase Transition in β' -Cu_xV₂O₅ and Its Structural Underpinnings

(A) Resistance versus temperature curve measured for an individual nanowire of β' -Cu_xV₂O₅. An optical micrograph of the device is shown in the inset. The scale bar represents 5 μ m (the nanowire has a width of approximately 330 nm). The right inset indicates an exponential fit with thermal activation energy of 120 meV for the insulating phase. See also Figure S2.

- (B) Differential resistance plots illustrating a voltage-driven metal-insulator transition. The second-derivative curve of the differential resistance plot is shown in the inset.
- (C) Resistance versus temperature plots measured as a function of current bias for an individual nanowire of β' -Cu_xV₂O₅ ($x \sim 0.50$). The insulator-to-metal transition (increasing temperature) is initiated at successively lower temperatures with increasing current bias.
- (D and E) High-resolution synchrotron X-ray diffraction data (gray circles) collected for β' -Cu_{0.55}V₂O₅ below (100 K), in the vicinity of (295 K), and well above (400 K) the metal-insulator transition. Rietveld refinement of the diffraction data is plotted as light blue (100 K), orange (295 K), and red (400 K) solid curves. The structure solutions obtained from Rietveld refinement of the patterns in (D) are shown in (E), represented as a 2 × 2 × 1 unit cells. Additional high-resolution powder X-ray diffraction data collected for β' -Cu_{0.35}V₂O₅, β' -Cu_{0.45}V₂O₅, and β' -Cu_{0.65}V₂O₅ are provided in Figure S7. Further details of these refinements are included in Supplemental Information (see Tables S1–S12).
- (F) A side-on view of the structure in (E) shows the arrangement of copper atoms (dark-blue polyhedra) along infinite chains within the tunnels of the V_2O_5 framework. Copper (light-blue

CellPress

Figure 1. Continued

atoms) is split between two sites within the tunnels (a central site, Cu(1) and a second site, Cu(2), which is reflected across the mirror plane represented in (G) as a dashed purple line). (G) The splitting of fractional copper occupancy between the Cu(1) and Cu(2) sites (shown as thermal displacement ellipsoids) results in a roughly triangular arrangement that lies in the (101) plane. The Cu(2) site is reflected across the mirror plane (C2/m), as highlighted by a dashed purple line

(H) With increasing temperature, the distribution of the Cu ions shifts from the Cu(1) to the Cu(2) site. The copper occupancies were obtained from high-resolution powder diffraction data and have approximate scatter in the third decimal place (shown as vertical error bars). The copper occupancies obtained from Rietveld refinement to β' -Cu_{0.35}V₂O₅, β' -Cu_{0.45}V₂O₅, and β' -Cu_{0.65}V₂O₅ patterns are tabulated in Table S14.

(NEB) calculations illuminate the coupled nature of the observed Cu-ion shuttling and polaron oscillation, further demonstrating that polaron oscillation between adjacent vanadium sites is facilitated by the observed Cu-ion diffusion, thereby driving the metal-insulator transition.

RESULTS AND DISCUSSION

Structural Underpinnings of the Electronic Phase Transition

Nanowires of β'-Cu_xV₂O₅ exhibiting a roughly rectangular cross-section (Figure S1) were synthesized according to a hydrothermal approach as described in Experimental Procedures and Supplemental Experimental Procedures. Figure 1A shows the electrical resistance of an individual β' -Cu_xV₂O₅ nanowire (x \sim 0.50, width of 330 nm, see also Figure S2) measured as a function of temperature. A pronounced thermally driven MIT is observed at 190 K upon heating; differential resistance plots in Figure 1B further indicate field-driven melting of the insulating state. Indeed, a small current of 4 µA triggers the insulator-to-metal transition, even at 135 K, which is well within the insulating regime. Figure 1C indicates the remarkable currentdriven transition induced within another individual nanowire device; each successive increase in current depresses the MIT to lower temperatures. Notably, Joule heating is unlikely to drive the transition, as the power dissipated is negligibly small (\sim 3 nW at 200 K). A linear relationship is observed between the thermal activation energy and \sqrt{I} , as shown in the inset to Figure 1C. Optical microscopy images, scanning electron microscopy images, and energy-dispersive X-ray spectra collected for individual nanowire devices are shown in Figure S2. Figures S2 and S3 further indicate that the critical MIT temperature (T_c) varies strongly as a function of the copper stoichiometry (i.e., x in β' -Cu_xV₂O₅) from 229 K for x \sim 0.46 to 171 K for x \sim 0.50 and 131 K for $x \sim 0.62$. These experiments show that T_c generally decreases with increasing copper content.²¹ The MIT appears to be entirely suppressed below x ~ 0.27 .

A reasonable test for a material that might be suitable for neuromorphic computing is to build a simple oscillator where the spacing between the oscillations is controlled by a capacitor. Such device function is imperative to realize nonvolatile nonlinear dynamical circuit elements that take advantage of an electrical instability in the current-voltage characteristics of the device to create gain in a circuit. ^{3,35–37} Figure S4 demonstrates the oscillating behavior of such an element incorporating a parallel capacitor (which can alternatively be the intrinsic capacitance of the device itself); the device is maintained at a constant resting potential in the high-resistance state and then responds as a "leaky integrate and fire" or "all-or-nothing" element by rapidly switching to a low-resistance state. Figure S4 not only demonstrates the switching function but illustrates that the material is both a natural oscillator and an amplifier within proximity of its electronic instability. The oscillation frequency



and damping are strongly affected by the value of the external resistor and the parasitic capacitance.

Figure S5 shows X-ray photoemission spectra (XPS) collected for β'-Cu_xV₂O₅ as a function of copper content. With increasing Cu content, a monotonic increase of the $V^{4+}/(V^{4+} + V^{5+})$ intensity ratio is observed. Reduction of vanadium is further verified by X-ray absorption near-edge spectroscopy (XANES) measurements in Figure S6, which show a monotonic diminution of spectral features derived from unoccupied V d_{xy} and $d_{xz/yz}$ states.^{29,31,33,38} High-resolution synchrotron powder X-ray diffraction measurements were performed for β' -Cu_xV₂O₅ (x = 0.55) nanowires across the phase transformation, as shown in Figure 1D. The corresponding structure solutions obtained from Rietveld refinement to the synchrotron diffraction data are shown in Figure 1E. The material retains its characteristic C2/m monoclinic symmetry across the discontinuous electronic transformation with complete retention of the quasi-1D tunnel structure and ordering of the Cu ions in 1D chains along the crystallographic b axis (Figure 1F). X-ray diffraction further reveals minimal perturbation of the shortest V-V distances across the phase transition, excluding the possibility that metallization occurs as a result of increased V 3d overlap (delineated in Table \$13);²⁷ the distances remain substantially greater than the critical 2.94-Å bond distance empirically determined by Goodenough as the threshold for metallization in vanadium oxides. Notably, however, with increasing temperature, a pronounced redistribution of the average position of Cu ions between two distinct crystallographic sites is observed (Figure 1G). In the β' -Cu_{0.55}V₂O₅ material, the two sites are occupied nearly equally at 100 K (Cu(1)/Cu(2), 0.52:0.48). However, upon heating to 400 K, the Cu ions have increased occupancy at the Cu(2) sites (Cu(1)/ Cu(2), 0.35:0.65) indicating temperature-driven shuttling of Cu ions between these two sites (Figures 1G and 1H). The monotonic increase in Cu(2) site occupancy with increasing temperature observed for β' -Cu_{0.55}V₂O₅ is similarly observed for other β' -Cu_xV₂O₅ compositions, as shown in Figure S7, Table S14 (refinement of high-resolution powder diffraction), and Table S15 (refinement of single-crystal diffraction).

To obtain a more detailed perspective of the temperature dependence of the Cu shuttling between the Cu(1) and Cu(2) sites, we grew single crystals of β'-Cu_xV₂O₅ as described in the Experimental Procedures section with intended stoichiometries of x = 0.35, 0.55, and 0.65 (intended and refined copper stoichiometries differ subtly for the obtained powders and selected crystals; see Table S14 for powder and Table S15 for single crystal). The extended crystal structure refined from a single crystal of β' -Cu_{0.65}V₂O₅ is shown in Figure 2A. Stacked layers of edge- and corner-sharing distorted VO₆ octahedra spaced by chains of edge-sharing VO₅ square pyramids give rise to a quasi-1D tunnel structure that hosts rows of Cu ions (inset, Figure 2A). The Cu ions in this structure exhibit static-site disorder, whereby any given Cu ion resides in one of two symmetry-inequivalent sites that are reflected across a mirror plane in the unit cell (Figure 1G), thereby constituting the triangular clusters of Cu interstitial sites shown in Figures 1H and 2A-2E. Single-crystal X-ray diffraction allows for the refinement of anisotropic displacement parameters, which are closely correlated with the fractional occupancies of these two Cu sites, as a function of temperature. Figure 2B depicts the anisotropic displacement of Cu ions in β'-Cu_{0.35}V₂O₅ at 110 K, whereas Figure 2C depicts the displacement within the same crystal at 250 K. At both high and low temperatures, the atomic displacement is relatively constrained parallel to the (010) mirror plane (Figure 1H); however, in the high-temperature structure, a significant increase of the lateral displacement is observed parallel to the (101) plane in which

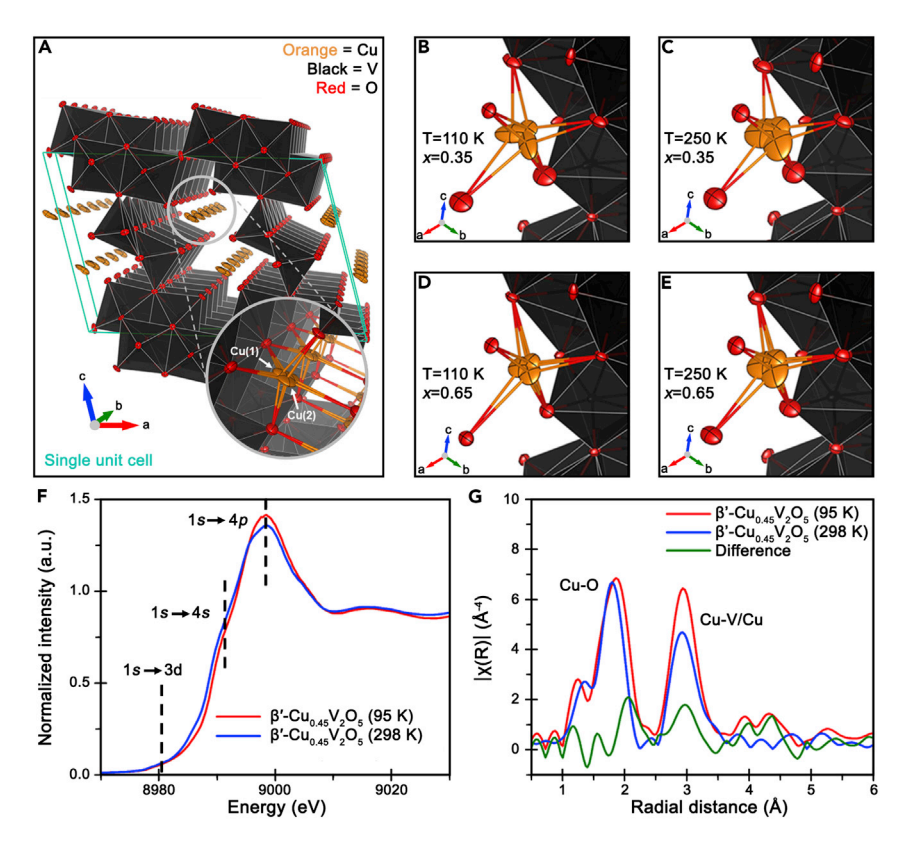


Figure 2. Cu-lon Shuttling Evidenced by Single-Crystal Diffraction and Extended X-Ray Absorption Fine Structure

(A) Crystal structure of β' -Cu_{0.55}V₂O₅, showing Cu split-site disorder along the tunnels of V₂O₅. Key: Cu, gold; O, red; V, black.

(B–E) Refined structures of β' -Cu_xV₂O₅ derived from single-crystal diffraction. Thermal ellipsoids are shown at 90% probability (key: Cu, gold; O, red; V, black). Cu polyhedra are omitted to show Cu split-site disorder and thermal ellipsoids. Refined structures of (B) β' -Cu_{0.35}V₂O₅ at 110 K; (C) β' -Cu_{0.35}V₂O₅ at 250 K; (D) β' -Cu_{0.65}V₂O₅ at 110 K; and (E) β' -Cu_{0.65}V₂O₅ at 250 K.

- (F) Comparison of Cu K-edge XANES spectra of $\beta'\text{-}\text{Cu}_{0.45}\text{V}_2\text{O}_5$ collected at 95 K and 298 K.
- (G) k^3 -weighted Fourier transforms of the Cu K-edge EXAFS spectra collected at 95 K (red curve) and 298 K (blue curve). The green curve shows the difference spectrum between the red and blue curves. A phase-correction term of 0.3 Å has been added to the R-space data. The fitted R-space and k-space EXAFS spectra acquired at 95 K and 298 K are shown in Figure S8; fitting parameters related to the major scattering paths are provided in Table S16.

the Cu-ion triangular cluster lies, reflecting greater thermal motion and increased spatial overlap between the distinct Cu positions. At higher Cu content (x = 0.65), the temperature dependence of the split occupancy of the two Cu positions is observed to change. Figure 2D depicts the Cu thermal ellipsoids in a crystal of β' -Cu_{0.65}V₂O₅ at 110 K, whereas Figure 2E depicts the structure of the same crystal determined at 250 K. Once again, there is a pronounced but anisotropic increase in thermal displacement from 110 K to 250 K. However, whereas the effect of temperature on the relative Cu site occupancy in the β' -Cu_{0.35}V₂O₅ structure (Figures 2B and 2C) is muted, a significant temperature-driven reordering of the Cu site occupancies is observed in β' -Cu_{0.65}V₂O₅. At 110 K, the refined occupancy of the Cu(1) position in β' -Cu_{0.65}V₂O₅ is 0.220 (34.30% total Cu) per V₂O₅, whereas that of the Cu(2) position is 0.421 (65.70% total Cu) per V₂O₅. At 250 K, the split distribution of Cu is shifted toward the secondary site; the occupancy of the Cu(1) site is reduced to 0.133 (20.83% of total Cu) per V₂O₅, whereas that of the Cu(2)



site correspondingly increases to 0.507 (79.17% of total Cu) per V_2O_5 . The relative occupancies observed as a function of temperature and Cu stoichiometry are summarized in Table S14 (powder diffraction) and Table S15 (single-crystal diffraction). It should be noted that while the Cu(1) and Cu(2) site occupancies obtained by refinement of powder and single-crystal diffraction differ slightly, in part due to slight differences in stoichiometry and the inclusion of anisotropic thermal displacement parameters in the refinement of single-crystal diffraction data, the overall trends in copper occupancy are self-consistent. An increase in the Cu(2) site occupancy and a corresponding decrease in the Cu(1) site occupancy coupled with increased overlap of the Cu-ion thermal parameters with increasing temperature suggests thermally activated migration of Cu ions between Cu(2) sites through the Cu(1) site. Such Cu-ion shuttling across the triangular regions is delineated in Figures 2C and 2E, and is clearly correlated with the observed conductance switching.

To further illuminate subtle changes in the local coordination environment of Cu ions in β' -Cu_{0.45}V₂O₅, we performed Cu K-edge XANES (Figure 2F) and EXAFS (Figure 2G) measurements at temperatures that span the MIT. Three prominent spectral regions are highlighted in the XANES spectra shown in Figure 2F: the pre-edge region centered at approximately 8,980.4 eV that derives from dipole-forbidden transitions from Cu 1s core states to Cu 3d states hybridized with O 2p states; the rising edge centered at approximately 8,991.2 eV that derives from transitions from Cu 1s to Cu 4s states hybridized with O 2p states; and the white-line absorption centered at approximately 8,998.4 eV that derives from transitions from dipole-allowed Cu 1s to Cu 4p states. 39,40 Subtle differences in the XANES spectra acquired for β' -Cu_{0.45}V₂O₅ at 95 K and 298 K are apparent (Figures 2F and S8A) and derive from alterations of the local symmetry of the intercalated Cu ions with temperature consistent with the X-ray diffraction results above, corroborating the importance of Cu-ion shuttling in underpinning the MIT. 41,42

Temperature-variant EXAFS spectroscopy was further used to examine the local structure across the MIT. 43 Figures 2G and S8B plot Cu K-edge EXAFS spectra collected for β' -Cu_{0.45}V₂O₅ at 95 K and 298 K. The oscillation function $\chi(k)$ is most strongly modified in the k-range of 8–13 Å⁻¹ (Figure S8B); concomitant changes in the Fourier transform functions plotted in real space are shown in Figure 2G. Two features in the Fourier transform curve are modified significantly with increasing temperature; the first feature corresponds to the Cu–O bond distance at approximately 1.9 Å, whereas the second feature corresponds to overlapping Cu–V/Cu bond distances at approximately 3.0 Å. Fourier transform plots of the EXAFS spectra measured for β' -Cu_{0.45}V₂O₅ (Figure 2G) indicate pronounced broadening of the Cu–O feature with increasing temperature, reflective of local disorder; furthermore, the intensity of the Cu–V/Cu feature is decreased with increasing temperature. Two additional correlations are observed at approximately 2.0 Å and 3.0 Å in the 95 K Fourier transform spectrum and are most clearly discernible in the difference spectrum (green).

To understand the scattering paths involved in the change in lineshape of the Cu–O peak and the decrease in intensity of the Cu–V/Cu peak with increasing temperature, we calculated the difference in intensity of the fitted Fourier transform spectra at 95 K and 298 K. The difference spectrum in Figure 2G (green curve) is further deconvoluted into components originating from the Cu ion being positioned exclusively at the Cu(1) (red curve) or at the Cu(2) (black curve) sites (as shown in Figure S9A). The redistribution of Cu to the Cu(2) sites is shown to profoundly modify the peaks at 1.95 Å and 3.0 Å (black curve), whereas the features centered at approximately



1.85 Å and 2.7 Å (red curve) show the most pronounced changes upon redistribution to the Cu(1) site. Consequently, the features at 1.9 Å and 3.0 Å serve as indirect measures of the Cu-ion occupancies at the two crystallographically inequivalent sites, suggesting that the difference spectrum shown in Figure 2G can best be understood as deriving from the increased shuttling of Cu between the interstitial sites. The crystallography and EXAFS data taken together therefore show that a thermally activated cation-shuttling mechanism occurs concomitantly with the MIT of β' -Cu_xV2O5. Importantly, and as discussed in the Introduction, it has been established that the diffusion of Li ions between adjacent lattice interstitial sites is strongly coupled to the oscillation of nearby polarons located on the V2O5 lattice. $^{28-30,34}$ As such, the observed shuttling of Cu between two adjacent sites is likely to have profound implications for the electronic structure of β' -Cu_xV2O5.

Mapping Electronic Structure across the Metal-Insulator Transition

We further used density functional theory (DFT) in conjunction with direct spectroscopic probes to explore possible electronic structure origins of the MIT observed for β' -Cu_xV₂O₅. Despite the substantial limitations of DFT in the treatment of strongly correlated systems and the intractability of this large dynamically evolving system to approaches such as dynamical mean field theory, the results provide a guide to interpretation of X-ray spectroscopy data. 25,44-48 It is worth noting that electron correlation profoundly affects electrostatic interactions and thereby determines the precise crystal structure that is adopted. 48 While DFT (or DFT+U) methods are unable to capture this rich interplay between electron correlation and structural preference, our ability to obtain high-resolution crystal structures from single-crystal data enables such calculations to be used to interpret spectral signatures. The total density of states (DOS) and the atom-projected density of states (PDOS) calculated for β' -Cu_xV₂O₅ as a function of increasing Cu content (x) are shown in Figures 3A and 3B. The valence band predominantly comprises O 2p states, whereas the conduction band is mostly V 3d in nature as reflected in XANES spectra (Figure S6). The conduction band is further split into a t_{2q} manifold derived from V $3d_{xy}$, $3d_{yz}$, and $3d_{xz}$ states undergoing π -type interactions with O 2p states and higher energy e_g^* states derived from V $3d_{z2}$ and $3d_{x2-y2}$ states interacting through σ interactions with O 2p states. ^{13,29,33} As a result of the significant distortion of the vanadium coordination environment away from octahedral geometry, the t_{2g} manifold is further split into a set of nondegenerate states positioning V $3d_{xy}$ and $3d_{vz}$ states at the bottom edge of the conduction band (Figure 3B). ^{29,33} The localization of electrons within these states and their strong coupling to the resulting lattice distortion results in the stabilization of a small polaron.²⁹ As the copper content increases, filled states begin to appear at the top-edge of the valence band, just below the Fermi level (Figure 3A). These filled polaronic states are derived predominantly from Cu 3d states hybridized with V 3d and O 2p states (Figure 3B). The increased population of the midgap states effectively decreases the band gap of the material (from approximately 1.45 eV in pristine ζ -V₂O₅ to approximately 0.27 eV in β' -Cu_{0.66}V₂O₅). In contrast to the weakly localized polaronic states observed previously in β' -Li_xV₂O₅, the polaronic states in β'-Cu_xV₂O₅ are considerably stronger in intensity owing to hybridization with Cu 3d states.^{29,33,49}

The occupied DOS and the binding energies of the core levels of ζ -V₂O₅ and β' -Cu_xV₂O₅ were experimentally probed by XPS. The evolution of the valence band (0–10 eV below the Fermi level) and the core levels of β' -Cu_xV₂O₅ as a function of the Cu stoichiometry are shown in Figure 3C.^{33,49} The XPS spectra further show that an increase in the intensity of the Cu 3 ρ band at centered at approximately 70 eV and an increase in intensity of the valence-band peak centered at approximately 1.4 eV are observed with increasing Cu-ion concentration

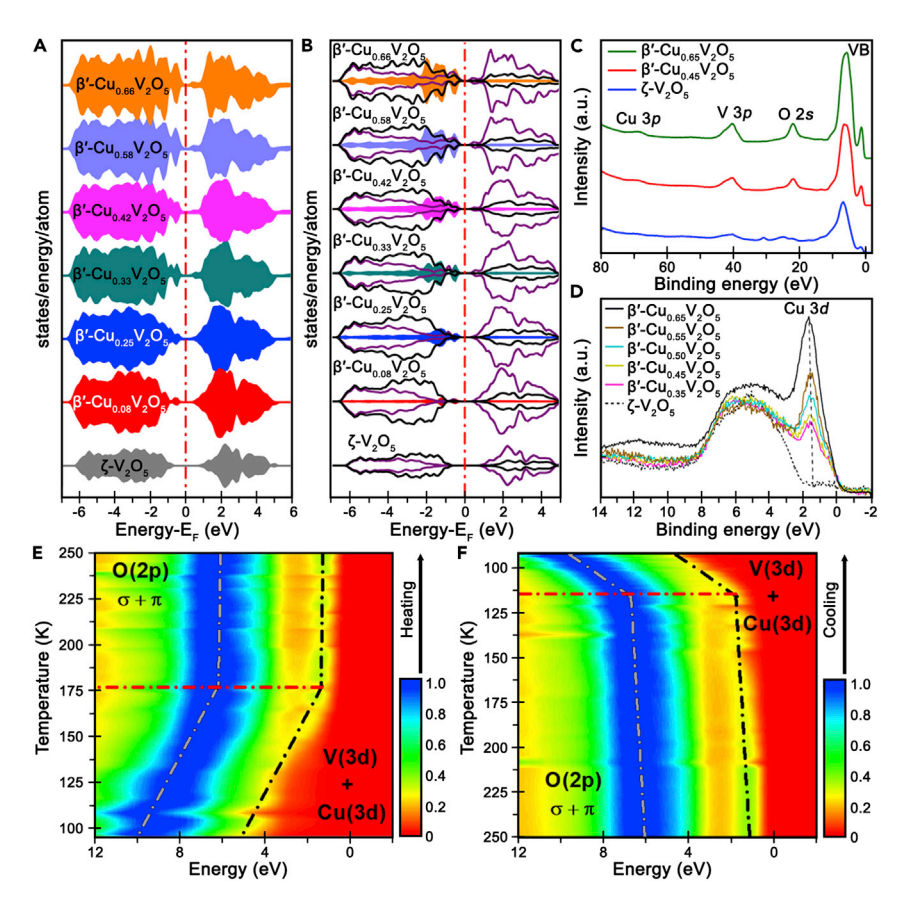


Figure 3. Electronic Structure Origins of the Metal-Insulator Transition in β' -Cu $_x$ V $_2$ O $_5$

(A and B) DFT+U calculated (A) total density of states and (B) atom-projected density of states for β' -Cu_x V_2O_5 as a function of Cu stoichiometry.

(C) Cu 3p, V 3p, and O 2s core-level valence-band XPS spectra collected for ζ -V₂O₅, β' -Cu_{0.45}V₂O₅, and β' -Cu_{0.65}V₂O₅.

(D) Valence-band XPS spectra acquired for ζ -V₂O₅ and β' -Cu_xV₂O₅ with intended stoichiometries of x=0.35, 0.45, 0.50, 0.55, and 0.65. A Cu 3*d*-derived "midgap" state is positioned at the upper edge of the valence band; this feature is absent in the binary ζ -V₂O₅ material and its intensity increases monotonically with increasing Cu content.

(E and F) Temperature-dependent angle-integrated valence-band photoemission spectra collected for β' -Cu_{0.45}V₂O₅, illustrating a discontinuous opening of the energy gap (E) at approximately 177 K during heating and (F) at approximately 115 K during cooling. A hysteresis of 62 K is observed.

See also Figure S10.

from x=0 to x=0.45 to x=0.65. A broad feature observed between binding energies of 0 eV and 8 eV is common to ζ -V₂O₅ and the β' -Cu_xV₂O₅ series and can be ascribed to O 2p states. ²⁹ Notably, a prominent feature centered at approximately 1.1 eV below the Fermi level is absent for ζ -V₂O₅ but monotonically increases with Cu stoichiometry in β' -Cu_xV₂O₅ (0.35 < x < 0.65). Based on the DFT+U calculations shown in Figures 3A and 3B, this feature can be attributed to Cu 3d states hybridized with occupied (polaronic) V 3d states. The X-ray emission spectra in Figure 3D thereby corroborate predictions from DFT for the role of Cu ions in diminishing the band gap of the material, which furthermore explains the decrease in T_c of the MIT temperature with increasing copper stoichiometry.

Temperature-variant angle-integrated valence-band photoemission spectroscopy measurements for β' -Cu_{0.45}V₂O₅ are shown in Figures 3E (heating) and 3F (cooling).



Analogous spectra collected for ζ -V₂O₅ and β' -Cu_{0.65}V₂O₅ are displayed in Figure \$10. Spectral features ascribed to the "midgap" hybrid Cu 3d-V 3d-O 2p and the O 2p states are delineated by black and gray dashed lines, respectively. During the heating cycle, an abrupt change in the spectrum is observed at approximately 177 K (red dashed line), denoting a discontinuous electronic transition. Specifically, an energy gap between the midgap and O 2p region (valence band) is seen to merge at high temperatures. During cooling (Figure 3F), a discontinuous transition and reversion of the spectrum to its initial state is observed at approximately 115 K, consistent with the observation of hysteresis in single-nanowire transport measurements. 10 In stark contrast, no such discontinuities are observed in the corresponding spectra acquired for ζ-V₂O₅ (which is devoid of Cu-ion-derived midgap states) in the temperature range between 80 K and 250 K (Figures \$10A and \$10B). A similar hysteretic discontinuity, albeit at lower temperature, is observed in angle-integrated valence-band photoemission spectra acquired for β'-Cu_{0.65}V₂O₅ (Figures S10C and S10D). The decrease in transition temperature with increasing Cu content observed in transport measurements (Figure S2) can thus be ascribed to the reduced effective band gap observed for increasing Cu content, as also deduced from the DFT+U calculations. The angle-integrated valence-band photoemission measurements thereby delineate that the Cu-ion shuttling and observed conductance switching is accompanied by a closing of the band gap.

Resonant inelastic X-ray scattering (RIXS) measurements were acquired for β' -Cu_{0.45}V₂O₅ (Figure 4) and β' -Cu_{0.65}V₂O₅ (Figure S11) nanowires to further investigate the temperature dependence of the O 2p-Cu 3d-V 3d-derived "midgap" states that appear at the upper edge of the valence band. Figure 4A displays the RIXS spectra acquired for β' -Cu_{0.45}V₂O₅ nanowires at the V L₃-edge, normalized to the maximum of the CT peak, alongside the corresponding XANES spectrum. The normalized V L₃-edge RIXS spectra were further plotted on an energy-loss scale, as shown in Figure 4B. When excited at 517.2 eV, which corresponds to the absorption onset, a broad feature emerges around approximately 511 eV on the emission scale and approximately -6 eV on an energy-loss scale. Based on the DFT+U calculations discussed above (Figure 3B), and by analogy to assignment from previous RIXS studies of V_2O_5 , β -Sr_{0.17} V_2O_5 , and α'/β -Na_x V_2O_5 , α'^{49-53} this feature can be ascribed to charge-transfer excitations between V 3d-O 2p hybrid states. Spectral features at -3 to -4 eV on the energy-loss scale (Figure 4B) are thought to originate from hybrid O 2p-Cu 3d-V 3d filled "polaronic" bands, as discussed above and predicted from the DFT+U calculations (Figure 3B). A sharp feature at approximately 516 eV in the emission spectrum and at -1.5 eV on an energy-loss scale is observed and is most pronounced upon excitation at 519.4 eV, which corresponds to resonant excitation at the V $3d_{xy}$ feature (Figures 4A and 4B). In accordance with previous literature, this feature can be ascribed to $d\text{-}d^\star$ transitions. ^{49,51–54} The temperaturevariant spectra plotted in Figure 4 reveal that the observed d-d* feature is reduced in intensity at 298 K ($T > T_{MIT}$) in comparison with 80 K ($T < T_{MIT}$), indicative of greater delocalization of the electrons with increasing temperature. These spectral features in conjunction with X-ray absorption result in Figure S6, and valence-band spectroscopy results in Figure 3C provide strong support for the formation and thermally driven delocalization of polarons.

Figures 4C and 4D sketch the V $2p \rightarrow 3d \rightarrow 2p$ RIXS processes as per a single-impurity Anderson model (AIM) formalism. ^{55,56} The observed RIXS spectra are consistent with the DFT calculations and are further characteristic of a Mott insulator. Vanadium cations in ζ -V₂O₅ can be assumed to have a +5 oxidation state and a $3d^0$ configuration. RIXS probes charge neutral excitations, and the only charge neutral

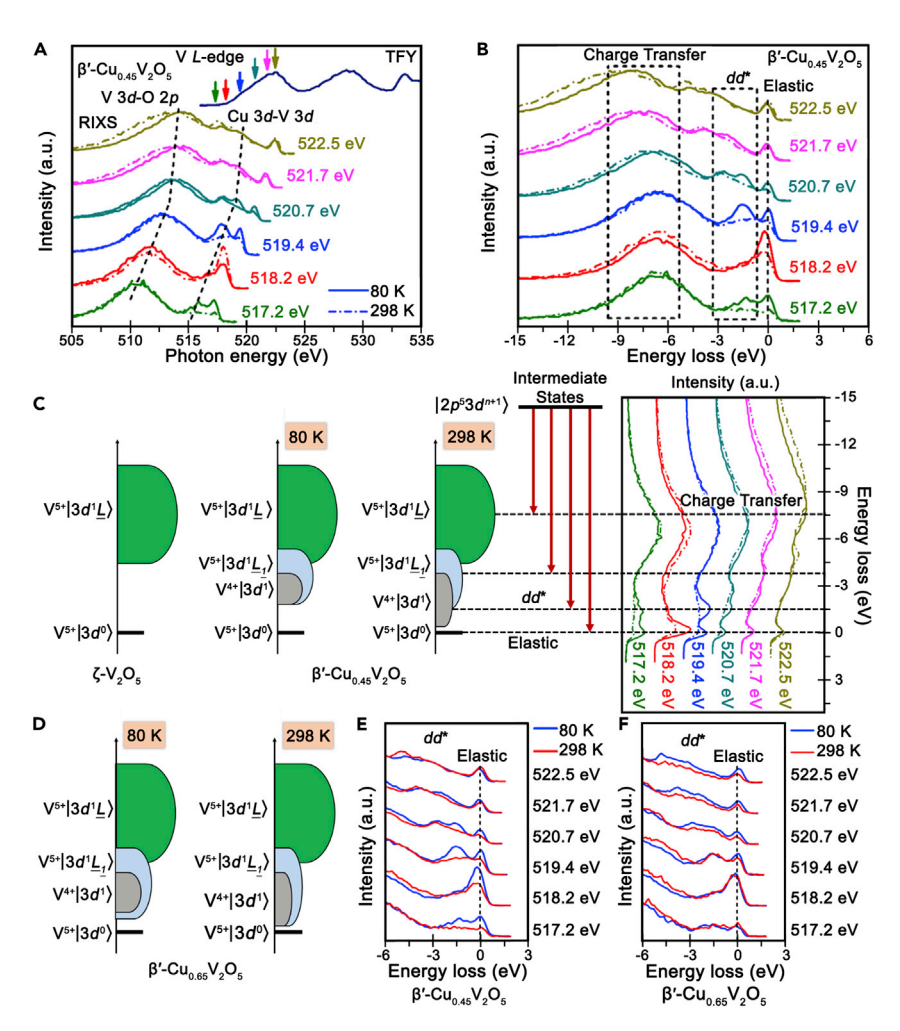


Figure 4. Temperature-Driven Delocalization of Polaronic States as Probed by Resonant Inelastic X-Ray Spectroscopy

(A) RIXS spectra collected at the V L_3 -edge for β' - $Cu_{0.45}V_2O_5$ nanowires. Spectra are normalized to the maximum of the CT peak, and the corresponding XANES (TFY) spectrum is shown as a dark-blue curve. The RIXS excitation energy is increased from the absorption onset toward the main V L₂edge, as indicated by colored arrows above the inset XANES spectrum. The normalized RIXS spectra are color-coordinated to the corresponding excitation energy arrows. (B–F) The normalized V L₃-edge RIXS spectra are further displayed on an energy-loss scale (B). A schematic representation of the V $2p \rightarrow 3d \rightarrow 2p$ excitations based on a single-impurity Anderson model is shown for (C) ζ –V₂O₅ and β' -Cu_{0.45}V₂O₅ and for (D) β' -Cu_{0.65}V₂O₅. In all instances, \underline{L} represents an electron transferred from the oxygen 2p valence band to V 3d states through pd hybridization, and L₁ represents an electron transferred from the hybridized Cu 3d-O 2p valence band to V 3d states through p-d hybridization. Note that the spectrum included in (C) to schematically illustrate the origins of the RIXS spectral features is the same as included in (B) for β' -Cu_{0.45}V₂O₅. Variable-temperature normalized V L₃-edge RIXS spectra displayed on an energyloss scale for (E) β' -Cu_{0.45}V₂O₅ and (F) β' -Cu_{0.65}V₂O₅. The spectra are plotted in the range -6 to 3 eV to highlight the observed d-d* transition. See also Figure S11.

oscillations possible in the AIM are from the full O 2p band to V $3d^0$ states. As a result of neutral charge fluctuations, this neutral excitation leads to the formation of a V⁵⁺| $3d^1\underline{L}$ band (green states in Figures 4C and 4D, wherein \underline{L} represents an electron transferred from the oxygen 2p valence band to the V 3d band through p-d hybridization), observed as charge-transfer excitations at approximately 6 eV on an energyloss scale (Figures 4C and 4D). In contrast to ζ -V₂O₅, β '-Cu_xV₂O₅ has additional Cu



3d states that hybridize with O 2p states. Neutral charge fluctuations in these states lead to the formation of a $V^{5+}|3d^1\underline{L}_1\rangle$ band (light-blue states in Figures 4C and 4D, wherein \underline{L}_1 represents an electron transferred from the hybrid Cu 3d-O 2p valence band to the V 3d state through p-d hybridization), observed as extended charge-transfer excitations at approximately -3 to -4 eV on an energy-loss scale. The positioning of these states above the O 2p band corroborates the classification of β' -Cu_xV₂O₅ as a Mott insulator. Furthermore, when Cu ions are intercalated within the V₂O₅ lattice, specific vanadium sites are reduced from a nominal +5 to +4 oxidation state, thereby yielding a mixed valence $3d^1/3d^0$ system. Consequently, additional $V^{4+}|3d^1\rangle$ states (Figures 4C and 4D) corresponding to d-d* transitions appear below the CT bands at approximately -1.5 eV on an energy-loss scale.

In the case of β' -Cu_{0.45}V₂O₅, the intensity of the d-d* feature is diminished at higher temperature (298 K, blue and cyan spectra in Figures 4A, 4B, and 4E). As sketched in Figure 4C, the $V^{4+}|3d^1\rangle$ band is more delocalized and has higher energy dispersion at 298 K as compared with 80 K. The diminution in the intensity of the d-d* feature can be understood by considering that the X-ray absorption cross-section is dependent on the coupling between the initial and the final state. ^{57,58} Since the initial 2p eigenstate on the V atom is localized, the most intense peak will be obtained for a final state that is also localized, which indeed appears to be the case at 80 K. However, the final states appear to have a weaker coupling with the initial states at 298 K and result in a substantially broadened d-d * feature (Figures 4C and 4D). RIXS spectra acquired for β'-Cu_{0.65}V₂O₅ nanowires are plotted in Figure S11. In other words, RIXS spectra show that electron localization (corresponding to polaronic states) on vanadium sites is strongly altered as a function of temperature and is further coincident with the shuttling of Cu ions as observed in crystallographic and EXAFS data. Higher temperatures induce greater Cu shuttling across the sites sketched in Figure 2, and this Cu-ion motion is correlated with greater delocalization of coupled polaronic states on the vanadium sublattice. The crystallography and EXAFS data in conjunction with RIXS and photoemission observations delineate the coupling between the thermally activated shuttling of Cu ions and delocalization of the polaronic states, which brings about a pronounced MIT.

Coupling of Ionic Diffusion and Electronic Structure Underpins the Metal-Insulator Transition in β' -Cu_xV₂O₅

MD simulations were used to investigate the electronic structure implications of the migration of Cu ions between the Cu(1) (symmetric) and the Cu(2) (asymmetric) sites as evidenced by X-ray diffraction (Figures 1 and 2) and EXAFS (Figure 2). Snapshots of the MD trajectory for the diffusion of one of the Cu ions between these sites in β' - $Cu_{0.33}V_2O_5$ are shown in Figures 5A–5C and are compiled in Video S1. The total DOS and the PDOS for the V atoms delineated V(9) and V(10) are shown in Figures 5D-5F. At 2.00 ps (Figure 5A), the Cu ion is in closer proximity to the V(10) atom with an approximate bond distance of 3.29 Å, whereas the Cu(1)-V(9) bond length is 3.56 Å. Analyzing the corresponding DOS and PDOS in Figure 5D reveals a band gap of approximately 0.56 eV for this configuration. In contrast, at 3.50 ps (Figure 5B), the Cu ion is positioned almost equidistant to the V(9) and V(10) atoms with Cu–V(10) and Cu–V(9) bond lengths of 3.63 Å and 3.56 Å, respectively. Interestingly, the DOS in Figure 5E reveals that the band gap of the material is almost entirely closed (a small band gap of approximately 0.05 eV is retained), reflecting transformation to a metallic state for this configuration. The corresponding PDOS in Figure 5E reveals that a significant contribution to the decrease in the band gap arises from the Cu ion being equidistant to the two V atoms. Finally, at 3.95 ps (Figure 5C), the Cu ion is again positioned in the asymmetric site; however, in contrast to

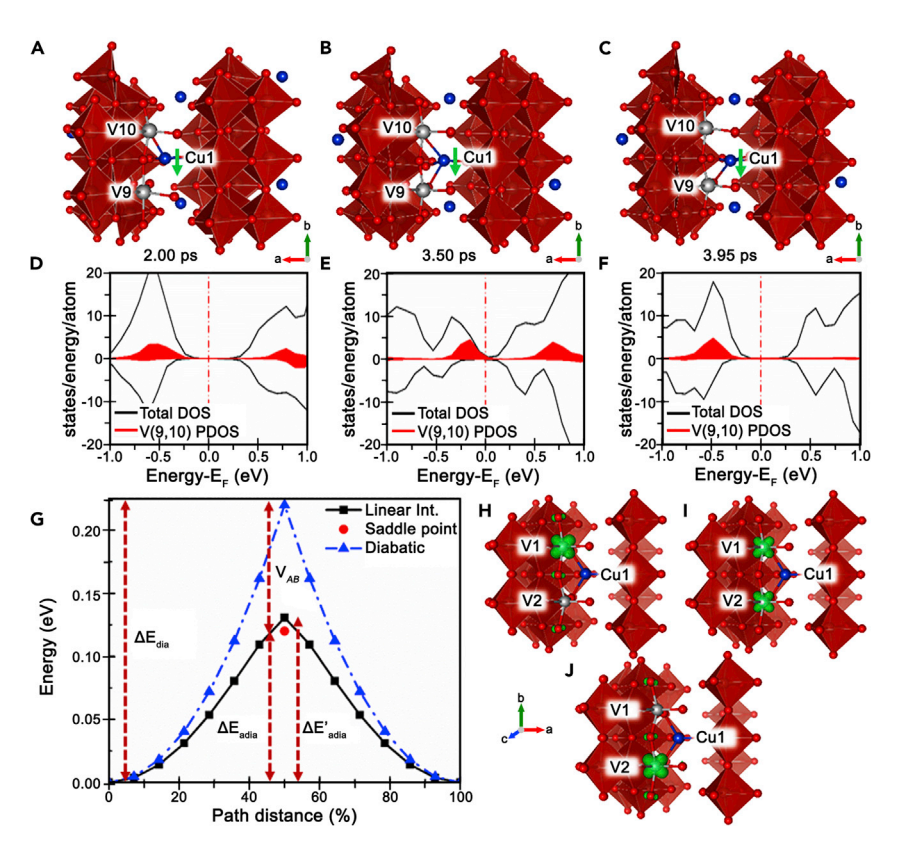


Figure 5. Coupled Polaron Oscillation and Cu-lon Shuttling in β' -Cu_xV₂O₅

(A–F) The migration of Cu ions between the Cu(1) and the Cu(2) sites of β' -Cu_{0.33}V₂O₅ was studied using molecular dynamics (MD) calculations. Snapshots of the MD trajectory for the diffusion of one of the Cu ions from (A) the Cu(2) site to (B) the Cu(1) site, and (C) back again to the Cu(2). The corresponding calculated total DOS and PDOS (solid red region) for the atoms labeled V9 and V10 are plotted in (D) to (F).

(G–J) The adiabatic and non-adiabatic diffusion barriers for the concomitant oscillation of polarons from V1 to V2 sites and shuttling of the Cu ion from Cu(1) to Cu(2) in β -Cu_{0.08}V₂O₅ are depicted (G), wherein (H) is the initial state, (I) is the transition state, and (J) is the final state. The dashed blue line in (G) shows the harmonic energy curve and its intersection represents the non-adiabatic energy barrier (ΔE_{dia}). The black line in (G) shows the adiabatic energy barrier, which is calculated along a reaction path defined by linear interpolation of the initial and final states. The red circle in (G) represents the relaxed saddle point geometry as calculated by NEB theory. See also Figures S12 and S13.

the configuration at 2.00 ps (Figure 5A), the Cu–V(10) bond length (4.02 Å) is longer than the Cu–V(9) (3.69 Å) bond length. Figure 5F illustrates the electronic structure consequences of this configuration, which results in a band gap of 0.46 eV. Analogous snapshots of diffusion trajectories and the corresponding PDOS for β' -Cu_{0.41}V₂O₅, are shown in Figure S12. The MD simulations thereby unify the diffraction data with the spectroscopic data, illustrating that the thermally activated diffusion of Cu ions (Figures 1 and 2) between the two adjacent Cu(2) sites is concomitant with polaron delocalization and metallization observed in RIXS and angle-integrated valence-band photoemission measurements, and suggests that this coupled diffusion of ions and polarons brings about metallization evidenced in transport measurements as conductance switching.

Figure 5G illustrates that the approximate adiabatic activation energy barrier ($\Delta E'_{adia}$) for Cu-ion migration calculated using linearly interpolated ionic positions



is 0.13 eV. In contrast, the diffusion barrier (ΔE_{adia}) calculated using the relaxed geometry of the transition state is slightly lower at 0.12 eV. These values are in close agreement with the diffusion barrier calculated for polaron diffusion in β -Li_{0.08}V₂O₅.³³ In turn, the diabatic activation energy barrier is found to be 0.22 eV. Consequently, for this system, adiabatic polaron transfer as shown in Figure 5 is energetically more favorable than diabatic polaron hopping by 0.1 eV. These results make a compelling case that the diffusion of the Cu ion is vital, as the electronic diffusion of the polaron is strongly coupled to the shuttling of the nearby Cu ion and the subsequent structural distortion of the V₂O₅ lattice. While single polaron migration has been examined here, previous studies on Mg_xV₂O₅ have revealed that the diffusion of multiple coupled polarons can somewhat increase the migration barrier.³⁰ In summary, at higher temperatures the shuttling of the Cu ions between the Cu interstitial sites is facile and readily enables the delocalization of coupled polarons. The electronic structure implication of the Cu shuttling and polaron diffusion is a decrease in the band gap of the material, bringing about a transformation to a metallic phase.

Conclusions

In conclusion, the MIT in β' -Cu_xV₂O₅ can be triggered by modulation of temperature, voltage, or current; the critical transition temperature is found to depend sensitively on the Cu-ion stoichiometry (x). The subtle structural distortions in β'-Cu_xV₂O₅ across the thermal MIT have been examined using synchrotron powder X-ray diffraction, single-crystal X-ray diffraction, and EXAFS spectroscopy. Cu ions are shown to exhibit a split-site disorder between two adjacent crystallographic sites; temperature-dependent X-ray diffraction data acquired for different Cu stoichiometries (x) in β' -Cu_xV₂O₅ indicate increased disorder and shuttling of Cu ions between the two sites at higher temperatures. Angle-integrated valence-band photoemission spectroscopy and RIXS evidence the evolution of the electronic structure of the material with temperature and further demonstrate the stabilization of polarons comprising electrons localized on the V₂O₅ framework at low temperature. Increasing polaron delocalization is observed at higher temperatures and is shown to be concomitant with and coupled to Cu-ion shuttling. Ab initio MD simulations and NEB calculations demonstrate that the shuttling of the Cu ions between the two sites is facile and readily enables the adiabatic diffusion of coupled polarons. The electronic structure implication of coupled thermally driven Cu shuttling and polaron oscillation is manifest as a decrease in the band gap of the material, thereby stabilizing a metallic phase. The results provide mechanistic insights into the close interplay of ionic diffusion and electronic structure in underpinning MITs of strongly correlated systems. Importantly, the mechanism described here does not incorporate a discontinuous structural transformation as observed in materials exhibiting Peierls' distortions; detailed structural studies indicate the absence of a change in lattice symmetry or a discontinuous alteration of V-V distances. Instead, Cu-ion shuttling is strongly enhanced with increasing temperature (as evidenced by the greater overlap of Cu thermal ellipsoids at higher temperatures), and the concomitant delocalization of polaronic states on the vanadium sublattice underpins metallization. The delocalization of polaronic states reflects a transition that is best described in the Mott limit. 9,59 The combination of strong electron-phonon coupling resulting in polaron formation and the associated disorder of Cu ions across adjacent interstitial sites has close parallels with conceptual frameworks developed to address Mooij correlations in disordered metals. 60,61 Fratini and coworkers have developed a microscopic theory using dynamical mean field theory (DMFT) approaches that allow for treatment of Anderson localization and strong electron-phonon coupling at a comparable level. The emergence of a pseudo-gap and the associated transference

CellPress

of spectral weight away from the Fermi energy developed within their framework harkens to the behavior observed here in $\beta'\text{-}Cu_xV_2O_5$, although the large size of the system renders it a difficult target for treatment by DMFT methods. The utilization of cation shuttling and polaron diffusion paves the way toward the use of ionic vectors with subtle structural distortions for obtaining conductance switching with minimal energy dissipation such as required for energy-efficient neuromorphic computing and sensing. Future work will focus on examining the influence of stress and finite size confinement in modulating the conductance switching mediated by this mechanism.

EXPERIMENTAL PROCEDURES

Additional details of experimental methods related to preparing β' -Cu_xV₂O₅ single crystals, processing of single-crystal/high-resolution powder X-ray diffraction data, scanning electron microscopy, X-ray photoelectron spectroscopy, and *ab initio* MD calculations are provided in Supplemental Experimental Procedures.

Preparation of β/β' -Cu_xV₂O₅ and ϵ -Cu_xV₂O₅ Nanowires

The Cu_xV₂O₅ nanomaterials described in this work were prepared through two distinctive approaches. In the first approach, β' -Cu_xV₂O₅ powders were synthesized using a high-temperature solid-state reaction. Cu metal powder (Alfa Aesar, 99.99%) and V₂O₅ powder (Beantown Chemical, 99.5%) were mixed in stoichiometric amounts (i.e., x in $Cu_xV_2O_5$ ranging from 0.35 < x < 0.65 and x = 1.0) and ball-milled (Spex mill, acrylic beads) for 30 min. The intimately mixed powders were next sealed in a quartz ampoule under vacuum. The ampoules were heated in a muffle furnace at 550°C for 72 h. The contents of the ampoules were then removed and ground using a mortar and pestle and again sealed within a quartz ampoule under vacuum. The remixed powder was further annealed within a muffle furnace at 550°C for 7 days to obtain phase-pure samples. Black or purple/black polycrystalline powders were obtained depending on the Cu stoichiometry. Phase-pure powders of β'-Cu_xV₂O₅ (x = 0.35, 0.45, 0.55, and 0.65) were then treated hydrothermally to obtain 1D nanowires. In a typical reaction, 300 mg of β' -Cu_xV₂O₅ powders, 1 mL of 2-propanol, and 15 mL of deionized water (18 M Ω ·cm⁻¹) were added to a 23-mL polytetrafluoroethylene autoclave liner, which was subsequently sealed within a stainless-steel autoclave (Parr Instruments). The sealed autoclave was heated to 210°C for 24 h and then allowed to cool to room temperature. The obtained black/purple powders were removed from suspension by filtration, washed with copious amounts of water and 2-propanol, and allowed to dry in air overnight.

Single-Nanowire Transport Measurements

Standard photolithographic techniques were employed to isolate individual nanowires of single-crystalline $\beta'\text{-}Cu_xV_2O_5$ and construct device architectures. In brief, prior to device fabrication, a Si/SiO2 substrate comprising a Si wafer passivated with a SiO2 oxide layer with a thickness of 300 nm was thoroughly cleaned by ultrasonication in acetone, methanol, and deionized water. $\beta'\text{-}Cu_xV_2O_5$ nanowire samples were dispersed in 2-propanol with the aid of ultrasonication. This dispersion was drop-cast onto the cleaned Si/SiO2 substrate. Individual nanowires were identified by optical microscopy and multiterminal devices were fabricated using standard photolithographic techniques. Typically, fabricated devices had a channel length of $\sim\!5~\mu\text{m}$ between the source and drain. Finally, Cr/Au layers (5 nm/70 nm) were deposited using an electron-beam evaporator. All transport measurements were performed in a two-terminal DC configuration using a liquid nitrogen cryostat using Lakeshore 330 temperature controller, SR 7265 lock-in amplifiers, and a Keithley 2400 SourceMeter under high vacuum. For resistance versus temperature



measurements (Figures 1A–1C and S2), the sweep rate was kept at 1 K min $^{-1}$. To demonstrate basic characteristics of the $\beta\text{-}Cu_xV_2O_5$ material as required for neuromorphic computing, we connected a $\beta\text{-}Cu_xV_2O_5$ single-nanowire device to an external load resistor (100 k Ω) and to a signal generator. A voltage pulse (100 kHz) was applied to the device in the insulating phase (160 K, below the MIT transition temperature) and oscillations in the voltage output were measured.

XANES and EXAFS Measurements

Cu K-edge XANES and EXAFS spectra were collected at the Advanced Light Source (ALS) bending-magnet beamline 10.3.2 (2.4–17 keV). The storage ring is operated at 500 mA and 1.9 GeV. A custom-made liquid nitrogen cryostage was used to collect the data at 95 K, whereas spectra at 298 K were measured by stopping the flow of liquid nitrogen. Spectra were collected in fluorescence mode in the energy rage 8,880–9,280 eV and 8,880–9,980 eV (up to $k \approx 16.0 \, \text{Å}^{-1}$) by continuously scanning the Si(111) monochromator. Cu foil was used as a calibration standard. LabVIEW custom software was used to perform deadtime correction, glitch removal, energy calibration, pre-edge subtraction, and post-edge normalization. ⁶² The Athena suite of programs in the IFEFFIT package was used for further processing of the data. Multishell least-squares parameter fitting of the Cu K-edge EXAFS data was performed using ARTEMIS module of IFEFFIT software package. 63 The photoelectron mean free path, scattering amplitude, and phase functions were calculated using the FEFF6 program. 64 Crystallographic data obtained from high-resolution synchrotron powder X-ray diffraction was used to build models of the Cu site with the Cu ion positioned at both Cu(1) and Cu(2) sites. Physical constraints were placed on the coordination numbers (based on the structure refined from XRD) to reduce the correlation between the best-fit parameters and improve the quality of the refinement.

Angle-Integrated Photoemission Spectroscopy Measurements

High-resolution angle-integrated photoemission spectroscopy was performed using the μ ARPES end station at the MAESTRO facility at beamline 7.0.2 of the ALS. This end station is equipped with a hemispherical VG Sienta R4000 analyzer. The synchrotron beam is estimated to have a lateral size of around 30–50 μ m. Powder samples of β' -Cu $_x$ V $_2$ O $_5$ nanowires were loaded onto the sample holder and placed within the ultrahigh vacuum chamber. For angle-integrated photoemission spectroscopy and XPS measurements, a 15- μ m field-of-view circular aperture in the electron-beam path was used to select an area of interest in the sample. The end station has a total energy resolution of ca. 20 meV. Photon energies of 100 eV were used to acquire the Cu 3p, V 3p, and O 2s core-level data, and a photon energy of 30 eV to collect the valence-band spectra. The chamber was equipped with a custom-designed heating stage to facilitate temperature-variant experiments. The temperature was varied between a range of 80 to 298 K across heating and cooling cycles.

X-Ray Emission and Absorption Spectroscopy

RIXS spectra were collected at the ultrahigh efficiency iRIXS end station of beamline 8.0.1.1 of the ALS. The beamline undulator and spherical grating monochromator supply a linearly polarized photon beam. The linear polarization of the incident beam is parallel to the scattering plane. RIXS spectra were acquired at specific excitation energies; the excitation energy value was first calibrated, then the emission energy was calibrated based on the elastic feature. The XANES data shown in this work are collected in total fluorescence yield mode. All the data were normalized to the beam flux measured by a clean gold mesh upstream of the end station. For collection of the RIXS spectra at 80 K the samples were cooled using liquid N_2 , whereas spectra at 298 K were measured by stopping the flow of liquid N_2 .



XANES measurements were acquired at RE/IXS beamline (10ID-2) of the Canadian Light Source. All measurements were performed using the impurity diffraction grating, which has a resolving power $\Delta E/E$ of 700 in the measured energy range (508–565 eV). The utilized REIXS end station is equipped with a microchannel plate detector and a silicon drift detector. Partial fluorescence yield spectra were obtained by averaging spectra across a 100-channel width centered on either the V L-edge or O K-edge emission lines. Prior to measurement, powder samples were dispersed and affixed to copper tape. X-ray emission spectra plotted on an energy-loss scale were adjusted to 0 by subtracting the excitation energy from the spectra.

Computational Methods

The initial coordinates for β' -Cu_xV₂O₅ were obtained from refinement of powder and single-crystal X-ray diffraction data. Electronic structure calculations were performed using DFT⁶⁵ as implemented in the Vienna Ab initio Simulation Package (VASP), 66,67 Electron exchange-correlation interactions were implemented by using the generalized-gradient approximation of Perdew, Burke, and Ernzerhof.⁶⁸ The projector-augmented wave formalism with a kinetic energy cutoff of 600 eV was used to describe the electron-ion interactions.⁶⁹ On-site Coulomb interactions were included by using the rotationally invariant DFT+U formalism of Dudarev et al. ⁷⁰ For vanadium and copper atoms, on-site Coulomb interaction parameters of U = 3.0 and 7.0 eV, respectively, were used. The U value for vanadium was determined by comparing the band gap calculated for ζ-V₂O₅ (Figure S14A) and its experimental electronic band gap measured in our earlier work.⁷¹ The band gap of β' -Cu_{0.10}V₂O₅ was then calculated at different values of U for both V and Cu atoms (Figure S14B) and compared with Figures 3E and 3F in order to deduce U parameters for both Cu and V atoms. A Γ -point centered Monkhorst-Pack reciprocal grid of 4 × 4 × 4 k-points was used for first Brillouin zone sampling in the DOS calculation; a 2 × 2 × 2 k-points reciprocal grid was used for relaxation of the structures. The structures were considered to be relaxed when each Cartesian force component was less than $0.03 \text{ eV } \text{Å}^{-1}$ unless otherwise noted.

The diffusion of the Cu ions and the concomitant diffusion of polarons were calculated by employing the NEB formalism as implemented in VASP. DFT+U calculations were employed to examine the energetics and migration energy barriers associated with diffusion pathways. The linearly interpolated midpoint of the initial and final structures was relaxed to find the geometry and energy of the transition state. The endpoints were relaxed until each Cartesian force component was less than $0.001~\text{eV}~\text{Å}^{-1}$, whereas for the forces along the NEB path the convergence criterion was $0.05~\text{eV}~\text{Å}^{-1}$. To discard spurious interactions between the images, we built the supercell such that the distance between the images was no less than 7.3~Å.

Cu-ion diffusion and the associated polaron diffusion on the vanadium centers were further modeled using NEB calculations. The Cu ion and its associated polaron at site V1 represents the initial ground-state configuration (labeled as 0 in Figure 5G). The final state of the system is related to the initial state by symmetry (labeled as 100 in Figure 5G). Hence, once the polaron is obtained on the initial ground-state geometry, a translational operation can be performed to obtain the coordinates of the final state. Figure 5G plots the diffusion-energy barrier versus the reaction coordinate for the diffusion of the polaron and the Cu ion from the initial to the final state. Three different scenarios have been considered for polaron diffusion. In the first case, as shown by the dashed blue line, change in energy as a function of change in ionic position keeping the polaron localized either on site 0 or site 100 is described by harmonic potential energy wells centered at sites 0 and 100. The intersection of these



harmonic potentials yields the non-adiabatic activation energy barrier ($\Delta E_{\rm dia}$). In this figure, we have plotted the harmonic potential energy wells using the calculated value of $\Delta E_{\rm dia}$:⁷²

$$\Delta E_{\text{dia}} = \Delta E_{\text{adia}} + V_{\text{AB}},$$
 (Equation 1)

where ΔE_{adia} is the adiabatic activation energy and V_{AB} is the electron coupling matrix element. According to the Mulliken-Hush formalism within the Marcus theory, ⁷³ the parameter V_{AB} was estimated as follows:

$$V_{AB} = \frac{1}{2} \Delta E_{12},$$
 (Equation 2)

where ΔE_{12} is the energy difference between the highest occupied state and the lowest unoccupied state of the adiabatic transition state. It should be noted that since we are using ground-state theory (DFT) to calculate the energy of the unoccupied state, the value of V_{AB} calculated here is approximate, but nevertheless illustrates the adiabaticity of polaron transfer. Figure S12 shows the total DOS and the PDOS of the relaxed transition-state geometry for atoms V1 and V2. The electron coupling matrix (V_{AB}) has been calculated to be 0.1 eV using the value of ΔE_{12} (0.2 eV), which is determined from Figure S12B.

In the second scenario, the approximate adiabatic activation energy barrier has been calculated by linearly interpolating the ion positions between states 0 and 100. Energies for the self-consistent charge densities on the Born-Oppenheimer surface correspond to these approximate ionic positions. The difference in energy calculated for the states 0 and 50, the linearly interpolated transition state, gives the value of approximate adiabatic activation energy barrier, denoted as $\Delta E'_{adia}$. Finally, in the third scenario, the linearly interpolated transition state is further relaxed using the NEB method to provide a refined transition-state geometry and with that the refined approximation of the adiabatic activation energy barrier, denoted as ΔE_{adia} .

Experimental details related to spin-polarized *ab initio* MD calculations are included in Supplemental Experimental Procedures.

SUPPLEMENTAL INFORMATION

Supplemental Information can be found online at https://doi.org/10.1016/j.matt. 2020.01.027.

ACKNOWLEDGMENTS

This work was supported primarily by the National Science Foundation under DMR 1809866. We also acknowledge support from the Qatar National Research Fund and the National Priorities Research Program, project number NPRP 10-0111-170152. We acknowledge the Texas A&M Supercomputing Facility for computational resources and the X-Grants Program of the President's Excellence Fund at Texas A&M University. DFT simulations were performed as part of a User Project with D.P. at The Molecular Foundry (TMF), Lawrence Berkeley National Laboratory. TMF is supported by the Office of Science, Office of Basic Energy Sciences, of the US Department of Energy, under contract no. DE-AC02- 05CH11231. A.P. acknowledges support from the Advanced Light Source (ALS) doctoral fellowship in residence. The ALS is supported by the Director, Office of Science, Office of Basic Energy Sciences, of the US Department of Energy, under contract no. DE-AC02-05CH11231. J.L.A. acknowledges support by a NASA Space Technology Research Fellowship grant no. 80NSSC17K0182. High-resolution synchrotron diffraction data were collected using the mail-in program at beamline 11-BM of the Advanced Photon Source. Use of the



Advanced Photon Source at Argonne National Laboratory was supported by the US Department of Energy, Office of Basic Energy Sciences, under contract no. DE-AC02-06CH11357. Use of the TAMU Materials Characterization Facility is acknowledged. Use of the TAMU Microscopy and Imaging Center is acknowledged.

AUTHOR CONTRIBUTIONS

Conceptualization, R.S.W., D.P., and S.B.; Methodology, A.P., J.V.H., J.L.A., J.W., S.S., C.J., A.B., E.R., W.Y., S.C.F., M.A.-H., G.S., L.F.J.P., R.S.W., D.P., and S.B.; Software, A.P. and D.P.; Formal Analysis, A.P., J.V.H., J.L.A., L.W., S.S., M.A.-H., G.S., L.F.J.P., R.S.W., D.P., and S.B.; Investigation, A.P., J.V.H., J.L.A., L.W., and S.S.; Resources, C.J., A.B., E.R., W.Y., and S.C.F.; Writing – Original Draft, A.P., J.V.H., J.L.A., D.P., and S.B.; Writing – Review & Editing, A.P., J.V.H., J.L.A., R.S.W., and S.B.; Visualization, A.P., J.V.H., and J.L.A.; Supervision, G.S., L.F.J.P., S.W., D.P., and S.B.; Project Administration, S.B.; Funding Acquisition, M.A.-H., D.P., and S.B.

DECLARATION OF INTERESTS

The authors declare no competing interests.

Received: August 26, 2019 Revised: November 30, 2019 Accepted: January 30, 2020 Published: February 26, 2020

REFERENCES

- Ionescu, A.M., and Riel, H. (2011). Tunnel fieldeffect transistors as energy-efficient electronic switches. Nature 479, 329–337.
- Salahuddin, S., Ni, K., and Datta, S. (2018). The era of hyper-scaling in electronics. Nat. Electron. 1, 442–450.
- Pickett, M.D., Medeiros-Ribeiro, G., and Williams, R.S. (2013). A scalable neuristor built with Mott memristors. Nat. Mater. 12, 114–117.
- Zhou, Y., and Ramanathan, S. (2013). Correlated electron materials and field effect transistors for logic: a review. Crit. Rev. Solid State Mater. Sci. 38, 286–317.
- Sarkar, D., Xie, X., Liu, W., Cao, W., Kang, J., Gong, Y., Kraemer, S., Ajayan, P.M., and Banerjee, K. (2015). A subthermionic tunnel field-effect transistor with an atomically thin channel. Nature 526, 91–95.
- Salahuddin, S., and Datta, S. (2008). Use of negative capacitance to provide voltage amplification for low power nanoscale devices. Nano Lett. 8. 405–410.
- Shukla, N., Thathachary, A.V., Agrawal, A., Paik, H., Aziz, A., Schlom, D.G., Gupta, S.K., Engel-Herbert, R., and Datta, S. (2015). A steep-slope transistor based on abrupt electronic phase transition. Nat. Commun. 6. 7812.
- Imada, M., Fujimori, A., and Tokura, Y. (1998). Metal-insulator transitions. Rev. Mod. Phys. 70, 1039–1263.
- Andrews, J.L., Santos, D.A., Meyyappan, M., Williams, R.S., and Banerjee, S. (2019). Building brain-inspired logic circuits from dynamically switchable transition-metal oxides. Trends Chem. 1, 711–726.

- Patridge, C.J., Wu, T.-L., Sambandamurthy, G., and Banerjee, S. (2011). Colossal above-roomtemperature metal-insulator switching of a Wadsley-type tunnel bronze. Chem. Commun. (Camb.) 47, 4484–4486.
- Andrews, J.L., De Jesus, L.R., Tolhurst, T.M., Marley, P.M., Moewes, A., and Banerjee, S. (2017). Intercalation-induced exfoliation and thickness-modulated electronic structure of a layered ternary vanadium oxide. Chem. Mater. 29, 3285–3294.
- Zavalij, P.Y., and Whittingham, M.S. (1999). Structural chemistry of vanadium oxides with open frameworks. Acta Crystallogr. B 55, 627–663.
- Parija, A., Waetzig, G.R., Andrews, J.L., and Banerjee, S. (2018). Traversing energy landscapes away from equilibrium: strategies for accessing and utilizing metastable phase space. J. Phys. Chem. C 122, 25709–25728.
- Marley, P.M., Horrocks, G.A., Pelcher, K.E., and Banerjee, S. (2015). Transformers: the changing phases of low-dimensional vanadium oxide bronzes. Chem. Commun. (Camb.) 51, 5181– 5198.
- Andrews, J.L., Singh, S., Kilcoyne, C., Shamberger, P.J., Sambandamurthy, G., and Banerjee, S. (2017). Memristive response of a new class of hydrated vanadium oxide intercalation compounds. MRS Commun. 7, 634–641.
- Ueda, Y. (1998). Vanadate family as spin-gap systems. Chem. Mater. 10, 2653–2664.
- 17. Ueda, Y., Isobe, M., and Yamauchi, T. (2002). Superconductivity under high pressure in $\beta(\beta')$ -

- vanadium bronzes. J. Phys. Chem. Solids *63*, 951–955.
- Marley, P.M., Singh, S., Abtew, T.A., Jaye, C., Fischer, D.A., Zhang, P., Sambandamurthy, G., and Banerjee, S. (2014). Electronic phase transitions of δ-Ag_xV₂O₅ nanowires: interplay between geometric and electronic structures. J. Phys. Chem. C 118, 21235–21243.
- Marley, P.M., Stabile, A.A., Kwan, C.P., Singh, S., Zhang, P., Sambandamurthy, G., and Banerjee, S. (2013). Charge disproportionation and voltage-induced metal-insulator transitions evidenced in P-Pb_xV₂O₅ nanowires. Adv. Funct. Mater. 23, 153–160.
- Patridge, C.J., Wu, T.L., Jaye, C., Ravel, B., Takeuchi, E.S., Fischer, D.A., Sambandamurthy, G., and Banerjee, S. (2010). Synthesis, spectroscopic characterization, and observation of massive metal-insulator transitions in nanowires of a nonstoichiometric vanadium oxide bronze. Nano Lett. 10, 2448– 2453.
- Onoda, M., and Sato, T. (2017). Polaronic nonmetal–correlated metal crossover system β'-Cu_xV₂O₅ with anharmonic copper oscillation and thermoelectric conversion performance. J. Phys. Soc. Jpn. 86, 124801.
- Yamaura, J.I., Yamauchi, T., Isobe, M., Yamada, H., and Ueda, Y. (2004). Observation of structural change with possible charge disproportionation in copper vanadium oxide bronze β'-Cu_{0.65}V₂O₅. J. Phys. Soc. Jpn. 73, 914–920.
- Yamada, H., and Ueda, Y. (2000). Structural and electric properties of β'-Cu_xV₂O₅. J. Phys. Soc. Jpn. 69, 1437–1442.



- 24. Stinson, H.T., Sternbach, A., Najera, O., Jing, R., Mcleod, A.S., Slusar, T.V., Mueller, A., Anderegg, L., Kim, H.T., Rozenberg, M., and Basov, D.N. (2018). Imaging the nanoscale phase separation in vanadium dioxide thin films at terahertz frequencies. Nat. Commun. 9, 3604.
- Nájera, O., Civelli, M., Dobrosavljević, V., and Rozenberg, M.J. (2017). Resolving the VO₂ controversy: Mott mechanism dominates the insulator-to-metal transition. Phys. Rev. B 95, 035113.
- Kalcheim, Y., Camjayi, A., del Valle, J., Salev, P., Rozenberg, M., and Schuller, I.K. (2019). Nonthermal resistive switching in Mott insulators. arXiv, 1908.08555. http://arxiv.org/abs/1908. 08555.
- 27. Goodenough, J.B. (1970). $M_xV_2O_5$ - β and M_xV_2 . $_yT_yO_5$ - β phases. J. Solid State Chem. 1, 349–358.
- Suthirakun, S., Genest, A., and Rösch, N. (2018). Modeling polaron-coupled Li cation diffusion in V₂O₅ cathode material. J. Phys. Chem. C 122, 150–157
- De Jesus, L.R., Horrocks, G.A., Liang, Y., Parija, A., Jaye, C., Wangoh, L., Wang, J., Fischer, D.A., Piper, L.F.J., Prendergast, D., and Banerjee, S. (2016). Mapping polaronic states and lithiation gradients in individual V₂O₅ nanowires. Nat. Commun. 7, 12022.
- Andrews, J.L., Mukherjee, A., Yoo, H.D., Parija, A., Marley, P.M., Fakra, S., Prendergast, D., Cabana, J., Klie, R.F., and Banerjee, S. (2018). Reversible Mg-ion insertion in a metastable one-dimensional polymorph of V₂O₅. Chem 4, 564–585.
- 31. Parija, A., Liang, Y., Andrews, J.L., De Jesus, L.R., Prendergast, D., Banerjee, S., Jesus, L.R., De Prendergast, D., and Banerjee, S. (2016). Topochemically de-intercalated phases of V₂O₅ as cathode materials for multivalent intercalation batteries: a first-principles evaluation. Chem. Mater. 28, 5611–5620.
- Koch, D., and Manzhos, S. (2019). Ab initio modeling and design of vanadia based electrode materials for post-lithium batteries. J. Phys. D Appl. Phys. 53, 083001.
- 33. Horrocks, G.A., Parija, A., De Jesus, L.R., Wangoh, L., Sallis, S., Luo, Y., Andrews, J.L., Jude, J., Fischer, D.A., Prendergast, D., et al. (2017). Mitigating cation diffusion limitations and intercalation-induced framework transitions in a 1D tunnel-structured polymorph of V_2O_5 . Chem. Mater. 29, 10386–10397.
- Watthaisong, P., Jungthawan, S., Hirunsit, P., and Suthirakun, S. (2019). Transport properties of electron small polarons in a V₂O₅ cathode of Li-ion batteries: a computational study. RSC Adv. 9, 19483–19494.
- Gibson, G.A., Musunuru, S., Zhang, J., Vandenberghe, K., Lee, J., Hsieh, C.C., Jackson, W., Jeon, Y., Henze, D., Li, Z., and Stanley Williams, R. (2016). An accurate locally active memristor model for S-type negative differential resistance in NbO_x. Appl. Phys. Lett. 108, 023505.
- Yi, W., Tsang, K.K., Lam, S.K., Bai, X., Crowell, J.A., and Flores, E.A. (2018). Biological plausibility and stochasticity in scalable VO₂

- active memristor neurons. Nat. Commun. 9, 4661.
- Bohaichuk, S.M., Kumar, S., Pitner, G., McClellan, C.J., Jeong, J., Samant, M.G., Wong, H.S.P., Parkin, S.S.P., Williams, R.S., and Pop, E. (2019). Fast spiking of a Mott VO₂carbon nanotube composite device. Nano Lett. 19, 6751–6755.
- 38. Andrews, J.L., Cho, J., Wangoh, L., Suwandaratne, N., Sheng, A., Chauhan, S., Nieto, K., Mohr, A., Kadassery, K.J., Popeil, M.R., et al. (2018). Hole extraction by design in photocatalytic architectures interfacing CdSe quantum dots with topochemically stabilized tin vanadium oxide. J. Am. Chem. Soc. 140, 17163–17174.
- Staniuk, M., Zindel, D., Van Beek, W., Hirsch, O., Kränzlin, N., Niederberger, M., and Koziej, D. (2015). Matching the organic and inorganic counterparts during nucleation and growth of copper-based nanoparticles—in situ spectroscopic studies. CrystEngComm 17, 6962–6971.
- Kumar, P., Nagarajan, R., and Sarangi, R. (2013). Quantitative X-ray absorption and emission spectroscopies: electronic structure elucidation of Cu₂S and CuS. J. Mater. Chem. C 1, 2448–2454.
- Gross, S., and Bauer, M. (2010). EXAFS as powerful analytical tool for the investigation of organic-inorganic hybrid materials. Adv. Funct. Mater. 20, 4026–4047.
- Guillerm, V., Gross, S., Serre, C., Devic, T., Bauer, M., and Férey, G. (2010). A zirconium methacrylate oxocluster as precursor for the low-temperature synthesis of porous zirconium(IV) dicarboxylates. Chem. Commun. (Camb.) 46, 767–769.
- Yao, T., Zhang, X., Sun, Z., Liu, S., Huang, Y., Xie, Y., Wu, C., Yuan, X., Zhang, W., Wu, Z., et al. (2010). Understanding the nature of the kinetic process in a VO₂ metal-insulator transition. Phys. Rev. Lett. 105, 226405.
- 44. Eyert, V. (2011). VO₂: a novel view from band theory. Phys. Rev. Lett. *107*, 016401.
- Mukherjee, S., Quackenbush, N.F., Paik, H., Schlueter, C., Lee, T.L., Schlom, D.G., Piper, L.F.J., and Lee, W.C. (2016). Tuning a straininduced orbital selective Mott transition in epitaxial VO₂. Phys. Rev. B 93, 241110.
- Brito, W.H., Aguiar, M.C.O.O., Haule, K., and Kotliar, G. (2017). Dynamic electronic correlation effects in NbO₂ as compared to VO₂. Phys. Rev. B 96, 195102.
- Lazić, P., Belashchenko, K.D., and Žutić, I. (2016). Effective gating and tunable magnetic proximity effects in two-dimensional heterostructures. Phys. Rev. B 93, 241401.
- Lanatà, N., Lee, T.H., Yao, Y.X., Stevanović, V., and Dobrosavljević, V. (2019). Connection between Mott physics and crystal structure in a series of transition metal binary compounds. NPJ Comput. Mater. 5, 30.
- Chen, B., Laverock, J., Newby, D., Su, T.-Y., Smith, K.E., Wu, W., Doerrer, L.H., Quackenbush, N.F., Sallis, S., Piper, L.F.J., et al. (2014). Electronic structure of β-Na_xV₂O₅ (x ≈ 0.33) polycrystalline films: growth,

- spectroscopy, and theory. J. Phys. Chem. C 118, 1081–1094.
- 50. Khyzhun, O.Y., Strunskus, T., Grunert, W., and Woll, C. (2005). Valence band electronic structure of V_2O_5 as determined by resonant soft X-ray emission spectroscopy. J. Eletron Spectrosc. 149, 45–50.
- Schmitt, T., Duda, L.-C.C., Matsubara, M., Augustsson, A., Trif, F., Guo, J.-H.H., Gridneva, L., Uozumi, T., Kotani, A., and Nordgren, J. (2004). Resonant soft X-ray emission spectroscopy of doped and undoped vanadium oxides. J. Alloys Compd. 362, 143–150.
- Zhang, G.P., and Callcott, T.A. (2006). Resolving dd transitions in NaV₂O₅ using angle-resolved resonant inelastic x-ray scattering at the V L edge. Phys. Rev. B Condens. Matter Mater. Phys. 73, 125102.
- 53. Laverock, J., Preston, A.R.H., Chen, B., McNulty, J., Smith, K.E., Piper, L.F.J., Glans, P.-A., Guo, J.-H., Marin, C., Janod, E., and Ta Phuoc, V. (2011). Orbital anisotropy and lowenergy excitations of the quasi-onedimensional conductor β-Sr_{0.17}V₂O₅. Phys. Rev. B Condens. Matter Mater. Phys. 84, 155103.
- Duda, L.C., Schmitt, T., Nordgren, J., Kuiper, P., Dhalenne, G., Revcolevschi, A., Zhang, G.P., Callcott, T.A., Woods, G.T., Lin, L., et al. (2004). Low-energy excitations in resonant inelastic Xray scattering of α'-NaV₂O₅. Phys. Rev. Lett. 93, 219701
- Kotani, A., and Shin, S. (2001). Resonant inelastic x-ray scattering spectra for electrons in solids. Rev. Mod. Phys. 73, 203–246.
- Bisogni, V., Catalano, S., Green, R.J., Gibert, M., Scherwitzl, R., Huang, Y., Strocov, V.N., Zubko, P., Balandeh, S., Triscone, J.-M.M., et al. (2016). Ground-state oxygen holes and the metal-insulator transition in the negative charge-transfer rare-earth nickelates. Nat. Commun. 7, 13017.
- Prendergast, D., and Galli, G. (2006). X-ray absorption spectra of water from first principles calculations. Phys. Rev. Lett. 96, 215502.
- Parija, A., Choi, Y., Liu, Z., Andrews, J.L., De Jesus, L.R., Fakra, S.C., Al-Hashimi, M., Batteas, J.D., Prendergast, D., and Banerjee, S. (2018). Mapping catalytically relevant edge electronic states of MoS₂. ACS Cent. Sci. 4, 493–503.
- Middey, S., Chakhalian, J., Mahadevan, P., Freeland, J.W., Millis, A.J., and Sarma, D.D. (2016). Physics of ultrathin films and heterostructures of rare-earth nickelates. Annu. Rev. Mater. Res. 46, 305–334.
- Ciuchi, S., Di Sante, D., Dobrosavljević, V., and Fratini, S. (2018). The origin of Mooij correlations in disordered metals. NPJ Quan. Mater. 3, 44.
- Di Sante, D., Fratini, S., Dobrosavljević, V., and Ciuchi, S. (2017). Disorder-driven metalinsulator transitions in deformable lattices. Phys. Rev. Lett. 118, 036602.
- 62. Kelly, S.D., Hesterberg, D., and Ravel, B. (2008). Analysis of soils and minerals using X-ray absorption spectroscopy. In Methods of Soil Analysis Part 5—Mineralogical Methods, A.L. Ulery and L.R. Drees, eds. (Soil Science Society of America), pp. 387–464.

Please cite this article in press as: Parija et al., Metal-Insulator Transitions in β' -Cu_xV₂O₅ Mediated by Polaron Oscillation and Cation Shuttling, Matter (2020), https://doi.org/10.1016/j.matt.2020.01.027

Matter



- Ravel, B., and Newville, M. (2005). ATHENA, ARTEMIS, HEPHAESTUS: data analysis for Xray absorption spectroscopy using IFEFFIT. J. Synchrotron Radiat. 12, 537–541.
- 64. Zabinsky, S.I., Rehr, J.J., Ankudinov, A., Albers, R.C., and Eller, M.J. (1995). Multiple-scattering calculations of x-ray-absorption spectra. Phys. Rev. B *52*, 2995–3009.
- **65.** Kohn, W., and Sham, L.J. (1965). Self-consistent equations including exchange and correlation effects. Phys. Rev. A *140*, 1133–1138.
- Kresse, G. (1995). Ab initio molecular dynamics for liquid metals. Phys. Rev. B 47, 558–561.
- 67. Kresse, G., and Furthmüller, J. (1996). Efficiency of *ab-initio* total energy calculations for metals

- and semiconductors using a plane-wave basis set. Comput. Mater. Sci. 6, 15–50.
- Perdew, J.P., Burke, K., and Ernzerhof, M. (1996). Generalized gradient approximation made simple. Phys. Rev. Lett. 77, 3865–3868.
- Kresse, G., and Joubert, D. (1999). From ultrasoft pseudopotentials to the projector augmented-wave method. Phys. Rev. B 59, 1758–1775.
- Dudarev, S., and Botton, G. (1998). Electronenergy-loss spectra and the structural stability of nickel oxide: an LSDA+U study. Phys. Rev. B Condens. Matter Mater. Phys. 57, 1505–1509
- 71. Tolhurst, T.M., Leedahl, B., Andrews, J.L., Marley, P.M., Banerjee, S., and Moewes, A.

- (2016). Contrasting 1D tunnel-structured and 2D layered polymorphs of V_2O_5 : relating crystal structure and bonding to band gaps and electronic structure. Phys. Chem. Chem. Phys. 18, 15798–15806.
- Adelstein, N., Neaton, J.B., Asta, M., and De Jonghe, L.C. (2014). Density functional theory based calculation of small-polaron mobility in hematite. Phys. Rev. B Condens. Matter Mater. Phys. 89, 245115.
- Reimers, J.R., and Hush, N.S. (1991). Electronic properties of transition-metal complexes determined from electroabsorption (Stark) spectroscopy. 2. Mononuclear complexes of ruthenium(II). J. Phys. Chem. 95, 9773–9781.